

PAPER • OPEN ACCESS

In vivo optogenetics using a Utah Optrode Array with enhanced light output and spatial selectivity

To cite this article: Niall McAlinden *et al* 2024 *J. Neural Eng.* **21** 046051

View the [article online](#) for updates and enhancements.

You may also like

- [A back-to-back diode model applied to van der Waals Schottky diodes](#)
Jeffrey Cloninger, Raine Harris, Kristine Haley et al.
- [Footprint tools tiptoeing towards nitrogen sustainability](#)
James N Galloway, Rachel E Michaels, Elizabeth A Castner et al.
- [Can the court bridge the gap? Public perception of economic vs. generational inequalities in climate change mitigation policies](#)
Nanna Lauritz Schönhage, Theresa Wieland, Luna Bellani et al.

Breath Biopsy Conference

BREATH BIOPSY[®]

Join the conference to explore the **latest challenges** and advances in **breath research**, you could even **present your latest work!**



5th & 6th November
Online



Main talks



Early career sessions



Posters

Register now for free!



PAPER

OPEN ACCESS

RECEIVED

13 March 2024

REVISED

24 July 2024

ACCEPTED FOR PUBLICATION

31 July 2024

PUBLISHED





14 August 2024

Original content from this work may be used under the terms of the [Creative Commons Attribution 4.0 licence](https://creativecommons.org/licenses/by/4.0/).

Any further distribution of this work must maintain attribution to the author(s) and the title of the work, journal citation and DOI.



In vivo optogenetics using a Utah Optrode Array with enhanced light output and spatial selectivity

Niall McAlinden^{1,5,*} , Christopher F Reiche^{2,5} , Andrew M Clark^{3,5}, Robert Scharf², Yunzhou Cheng¹, Rohit Sharma², Loren Rieth⁴, Martin D Dawson¹ , Alessandra Angelucci^{3,6}, Keith Mathieson^{1,6}  and Steve Blair^{2,6}

¹ SUPA, Institute of Photonics, Department of Physics, University of Strathclyde, Glasgow, United Kingdom

² Department of Electrical and Computer Engineering, University of Utah, Salt Lake City, UT, United States of America

³ Department of Ophthalmology and Visual Science, Moran Eye Institute, University of Utah, Salt Lake City, UT, United States of America

⁴ Department of Mechanical, Materials and Aerospace Engineering, West Virginia University, Morgantown, WV, United States of America

⁵ Joint first authors

⁶ Joint senior authors.

* Author to whom any correspondence should be addressed.

E-mail: niall.mcalinden@strath.ac.uk

Keywords: optogenetics, μ LED, optical modelling, neurotechnology, non-human primate

Supplementary material for this article is available [online](#)

Abstract

Objective. Optogenetics allows the manipulation of neural circuits *in vivo* with high spatial and temporal precision. However, combining this precision with control over a significant portion of the brain is technologically challenging (especially in larger animal models). **Approach.** Here, we have developed, optimised, and tested *in vivo*, the Utah Optrode Array (UOA), an electrically addressable array of optical needles and interstitial sites illuminated by 181 μ LEDs and used to optogenetically stimulate the brain. The device is specifically designed for non-human primate studies. **Main results.** Thinning the combined μ LED and needle backplane of the device from 300 μ m to 230 μ m improved the efficiency of light delivery to tissue by 80%, allowing lower μ LED drive currents, which improved power management and thermal performance. The spatial selectivity of each site was also improved by integrating an optical interposer to reduce stray light emission. These improvements were achieved using an innovative fabrication method to create an anodically bonded glass/silicon substrate with through-silicon vias etched, forming an optical interposer. Optical modelling was used to demonstrate that the tip structure of the device had a major influence on the illumination pattern. The thermal performance was evaluated through a combination of modelling and experiment, in order to ensure that cortical tissue temperatures did not rise by more than 1 °C. The device was tested *in vivo* in the visual cortex of macaque expressing ChR2-tdTomato in cortical neurons. **Significance.** It was shown that the UOA produced the strongest optogenetic response in the region surrounding the needle tips, and that the extent of the optogenetic response matched the predicted illumination profile based on optical modelling—demonstrating the improved spatial selectivity resulting from the optical interposer approach. Furthermore, different needle illumination sites generated different patterns of low-frequency potential activity.

1. Introduction

Optogenetics has made transformational contributions to neuroscience, enabling experiments that can dissect the roles of specific components in neural circuits [1]. Recently, the technique has been

translated to clinical trials, where it was used to partially restore light perception in blind patients [2]. The technique relies on several disciplines, including protein and genetic engineering for the development and delivery of light-sensitive ion channels, ion pumps and other neural modulators [3].

Photonic engineering also plays an important role in the development of methods to deliver light to neural substrates through highly scattering tissue with the required spatial and temporal resolution [4].

Advances in optogenetics have progressed rapidly, predominantly focusing on the mouse model. However, progress has not been as rapid in models that lack the sophisticated genetic tools and constructs developed for mice, such as the non-human primate [5–8]. Extending optogenetic methods to primate models is important to increase our understanding of neural functions in brains more similar to humans, and as an essential large animal test-bed towards further clinical translation. In addition to the development of opsin delivery toolkits, light delivery methods used in mouse models are not always adequate for the larger primate brain, where neural circuits require optical targeting spread over an increased volume [9, 10]. For experiments where only a single light source is required, current tools consisting of a single optical cannula coupled to an LED or laser are sufficient, as long as care is taken to not exceed phototoxic levels [11]. However, the delivery of patterned or multi-site illumination is more challenging. μ LED probes [12–16] and waveguide devices [17, 18] that work well in mouse studies do not provide light over a broad enough spatial extent for studies in larger mammals [8].

Surface illumination strategies [19–23] have been shown to work in primates, but light penetration depths are limited to less than 1 mm due to scattering and absorption in brain tissue [20]. For studies requiring deeper illumination, important in larger animal models as cortical thickness is typically in excess of 1 mm, several groups have developed penetrating microneedle devices [24, 25]. However, without an integrated light source, the animal must remain head fixed so that optical alignment can be maintained [26]. Other researchers have demonstrated that it is possible to insert multiple fibre optics [27] to achieve patterned light for deep structures, but again maintaining alignment of an external light source is required.

Previously, we reported on the Utah Optrode Array (UOA) [28], a light delivery device that addresses these issues. It consists of a matrix of μ LEDs, which is coupled to an array of microneedles, creating a device that can provide optogenetic illumination from 181 individual sites both to deeper layers (needles sites) and the surface of the cortex (interstitial sites). As the μ LED source and penetrating needles are directly coupled, optical alignment is maintained by the fabrication process. However, inefficiencies in optical coupling remain a significant challenge, due primarily to the Lambertian nature of μ LED emission, where total optical efficiencies (internal μ LED to target site) can be as low as 0.2%. This means that the μ LED needs to be driven with

drive currents of 10–100 mA (to deliver enough light to exceed typical optogenetic activation thresholds), which in turn means short pulse widths or low duty cycles are required to ensure the device remains within safe thermal limits. The Lambertian emission profile also means that optical crosstalk between stimulation sites can be problematic, creating ambiguities in the exact volume of tissue activated and reducing the applicability of the device to neuroscience experiments. Improving this coupling is central to enabling an optoelectronic, multi-site device that can provide spatially discrete optogenetic activation and operate at a high dynamic range (irradiance and duty cycle) without heating the brain by more than 1 °C [29, 30].

2. Methods

2.1. Optical modelling

To optimise the device design and fabrication, an optical model was created. This model was also used to understand light spread in tissue. Optical ray-tracing software (Zemax-Optics Studio 12, non-sequential mode) was used. Brain tissue was modelled using a Henyey–Greenstein scattering model, with a scattering coefficient of 10 mm⁻¹, an absorption coefficient of 0.07 mm⁻¹, and an anisotropy of 0.88 [31, 32]. To generate the cross-section images from simultaneously illuminated μ LEDs, the light output from a single needle was duplicated, spatially translated, and then summed with the output from other needles. The peak optical power out of each needle was then measured experimentally, for a given current/voltage, and used as an input to the model. This allowed for experimental variations in device optical output to be accommodated within the simulated results. To confirm that the optical modelling accurately reproduced experimental results, the optical output was measured by imaging the emission profile in fluorescein and compared with the modelled output.

2.2. Device fabrication—UOA

The implantable optogenetic device described here consists of two components: a glass needle array and a μ LED array. The Optrode Array and the μ LED array are fabricated separately and integrated during a final device assembly step. The completed device with a single μ LED illuminated is shown in figure 1(A).

The fabrication of the UOA is illustrated in figure 1 (with a schematic in figure A1). A 100 μ m thick silicon wafer is anodically bonded to a 2 mm-thick borosilicate glass wafer (figure 1(B)). The Si wafer will form the optical interposer, with the glass wafer being processed into the optical needle array. The anodic bonding was achieved at 350 °C, in a low vacuum (10⁻³ mbar), with a force of 2000 N, and a potential difference across the sample of 1000 V for 20 min using an EVG 520IS, (EVG, Austria). A thick photoresist (AZ9260, MicroChemicals) was

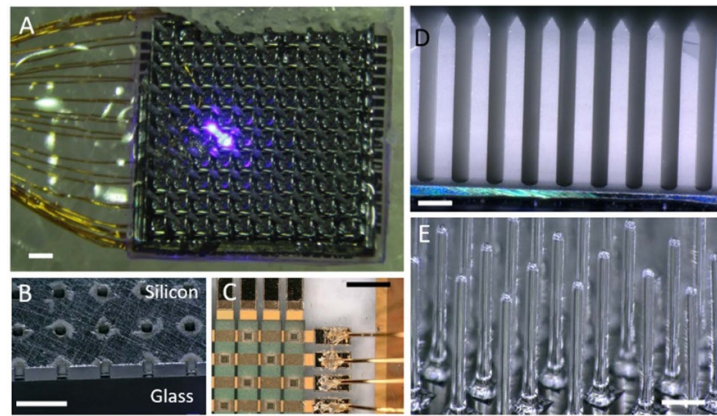


Figure 1. (A) Image of the completed device with a single μ LED illuminated (4 mm device width). (B) Cross-section image of silicon interposer with through-silicon vias (TSVs), anodically bonded to the glass Optrode base. In this example, TSVs were not opened for interstitial sites. (C) Image of a portion of the μ LED device. Wire bonds are visible on the right-hand side of the image. (D) Optrodes after dicing to reveal the needle shape. (E) Finished Utah Optrode Array. The glass needles were chemically etched to reduce their diameter to $110\ \mu\text{m}$ and thermally treated to smoothen their surface. All scale bars are $400\ \mu\text{m}$.

spin-coated on the silicon and standard photolithographic techniques were used to pattern arrays of $80\ \mu\text{m}$ diameter holes forming the mask for through-silicon via (TSV) etching. The TSVs were etched using the Bosch deep reactive ion etching process in a 100 ICP, Oxford Instr. Figure 1(B) shows the fully etched interposer array. After this step, the glass wafer-interposer combination is typically diced and subdivided into smaller dies for the subsequent needle dicing steps.

The UOA fabrication is adapted from previous processes [24] and starts with the glass/silicon interposer wafer. A bevelled dicing saw blade is used to cut the pyramidal-shaped optrode tips into the glass. By using blades with different bevel angles the pyramid angle can be adjusted to produce the desired tip shape and hence light emission profile. The optrode needles are then defined using a straight dicing blade performing cuts with a pitch of $400\ \mu\text{m}$, an edge width of $200\ \mu\text{m}$ and a height of approximately $1.6\ \text{mm}$, leaving a thin glass backplane (which is mostly removed in the subsequent etch step but is important to form the slightly larger base of the optrodes ensuring their stability). This process can be used to create optrode arrays with a range of dimensions, in this case, 10×10 arrays were produced. Using thicker blades, it is in principle possible to create optrode needles with even smaller edge widths (thinner). However, processing constraints mean that thinner optrodes are more likely to break during the dicing process. Figure 1(D) shows the needles after dicing on the interposer device, note the optically scattering sidewalls.

To prevent the interposer holes from filling with etchant during the next steps, the die is then mounted onto a carrier wafer using WaferGrip (Dynatex International). A 9:1 mix of hydrofluoric acid (concentration of 49%) and hydrochloric acid

(concentration of 37%) is used to thin the optrodes to their desired target width. In the proof-of-principle *in vivo* experiment, optrodes with a diameter of $110\ \mu\text{m}$ were used. This gives a well-controlled process with an etch rate of approximately $6\ \mu\text{m}\ \text{min}^{-1}$ at room temperature. After etching, the devices are rinsed with deionized water, removed from the carrier wafer, and cleaned from WaferGrip residues using successive baths of heated xylenes ($120\ ^\circ\text{C}$), *n*-butyl acetate (NBA), isopropanol (IPA) and deionized water.

Finally, the cleaned array batch is subjected to thermal treatment under vacuum in a muffle furnace. The device was heated to $560\ ^\circ\text{C}$ and held for 1 h to remove stress from the dicing steps. It is then heated to $725\ ^\circ\text{C}$ and held for 2 h which causes some glass surface reflow and gives an optically smooth surface to the needles (figure 1(E)). Before annealing, scattering from needle sidewalls resulted in almost no emission from the needle tip. After annealing, the glass surfaces become optically smooth and scattering in the needle sidewalls becomes negligible [24, 33]. During the annealing step, there is a noticeable geometry change including a slight rounding of the corners of the optrodes and a reduction of their length. Extended annealing causes further rounding of the tips, which could be used to change the light emission properties of the device (figures 2(F) and (G)). The further annealing does not affect the scattering along the needle sidewall [24, 34]. After this step, the device is again held at $560\ ^\circ\text{C}$ for 1 h to relieve stress in the glass that forms during cooling and then left to cool to room temperature. Finally, the die can be singulated with a dicing saw into individual UOAs, followed by a final cleaning step to remove any contamination from mounting the die during dicing. A completed needle array is shown in figure 1(E). The final needle lengths were $1.5\ \text{mm}$. Needles of between

0.5 and 2 mm can be achieved by modifying the dicing and annealing steps [24].

2.3. Fabrication— μ LED array

The μ LED array is fabricated on a commercial InGaN/GaN wafer. The III-nitride materials are grown on a c-plane (0001) 2 inch sapphire substrate. The GaN layers consist of an undoped GaN buffer layer, an n-type GaN layer and a multi-quantum well layer consisting of layers of InGaN and GaN designed to emit light at 450 nm. The MQW region is covered by an electron-blocking layer (*p*-type AlGaIn), to help confine electrons to the MQW region.

The fabrication process flow of the μ LED is detailed in [28] and discussed briefly here. Initially, electron beam evaporation is used to deposit a 100 nm-thick palladium current spreading layer on top of the *p*-type region. To ensure a good ohmic contact between the palladium and GaN the device is annealed at 400 °C for 3 min in a N₂ ambient. An inductively coupled plasma (ICP) process (Ar:Cl, 10:30 sccm flow) is used to etch mesa structures in the *p*-type layer (masked by a 300 nm PECVD silicon oxide layer) exposing the *n*-type GaN layer and defining the μ LED pixels. A Ti:Au metal stack (100:300 nm) is sputter deposited to create tracks connecting to the *n*-type region. A thin film passivation layer (1000 nm PECVD silicon dioxide) covers these tracks and *n*-type regions, with vias etched (Ar-fluoroform mixture in a reactive ion etch tool) to open electrical contact sites to the *p*-mesa. A second metal layer is then deposited to connect to the *p*-type regions (Ti:Au 50:300 nm). A further 300 nm of PECVD silicon dioxide protects the surface, with a further RIE step to open the bond pad sites around the periphery of the device (see figure 1(C)). Bond pads have an additional Ti:Pt:Au (100:200:400 nm) layer sputter deposited to improve the wire bonding yield.

2.4. Device fabrication—integration and encapsulation

Integration of the device was completed using a flip-chip bonder (Fineplacer pico-2, Fintech). The glass needle array was held in a custom-made holder and the μ LED array was brought to within 10 μ m of the UOA. Imaging was used to ensure accurate alignment. An underfill capillary gap-filling method was used to dispense the UV curable glue (Norland 61) as this ensured no air bubbles and gave the best overall alignment. Optical modelling was used to determine the misalignment tolerance (appendix 2). This indicates that there is little loss in optical coupling efficiency for misalignments up to 20 μ m.

Developing an electrical connection scheme to address each μ LED separately is challenging in terms of track routing and number of bond pad sites. Therefore, a matrix-addressing scheme was adopted. In this approach, all pixels along one column

share a common anode (*p*-contact) and all pixels along one row share a common cathode (*n*-contact). Therefore, 38 connections are required, 19 anodes and 19 cathodes, which simplifies the electronic driver scheme dramatically compared to individually addressed μ LEDs. This approach allows commercial LED current drivers to be employed, and reduces the number of connections, at the cost of limiting the available patterns that can be displayed. For example, individual μ LEDs, horizontal or vertical lines and rectangles/squares are possible. Diagonal light patterns and simultaneously displayed horizontal and vertical lines are not possible unless pulse width modulation schemes are used to realise these restricted patterns (see supplementary movie 1).

Each of the 38 connections is linked to LED driver circuitry through insulated gold wire bonds (25 μ m diameter and up to 10 cm long). The bond pads and wire bonds were then coated in silicone and Parylene-C was deposited to further encapsulate the device. The finalised device, with a single needle site switched on, is shown in figure 1(A).

2.5. Electrical and thermal characterisation

To ensure device stability and quantify the optical coupling efficiency, the output from each μ LED was characterized electrically and optically, before and after final integration. Before integration, this was done using a programmable power supply (B2901A, Keysight Technologies) and optical power meter (S120VC, Thorlabs). Since the optical power meter has a limited collection aperture (a diameter of 9.5 mm), a geometric correction factor was used to calculate the total optical power emitted by the μ LED. We previously benchmarked this setup against μ LED devices measured in an integrating sphere to quantify the correction factor. For the optical power meter setup, the μ LED to detector distance was 10 mm. Optical modelling of this geometry indicated that the detector would collect 1.5% of the light generated in the mesa structure of the μ LED. Most of the losses are due to the high refractive index of GaN (2.37) and Sapphire (1.76) meaning up to 90% of the light generated is trapped by total internal reflection in the device [35] or emitted out the side of the sapphire substrate. After integration, the completed device was tested in an integrating sphere. This measurement collected 100% of the light emitted from the tip of the device and confirmed the 0.4% optical efficiency (internal μ LED to needle tip) predicted by optical modelling. The thermal performance of the device was measured in air using an infrared camera (SC7000, FLIR).

Thermal modelling using finite element analysis (FEA) software (COMSOL Multiphysics) allowed the thermal measurements in air to be related to device performance *in vivo*. A geometrical model

Table 1. Thermal properties used in the FEA simulations.

| Material | Thermal conductivity ($\text{W m}^{-1} \text{ } ^\circ\text{C}^{-1}$) | Heat capacity ($\text{J}^{-1}\text{kg } ^\circ\text{C}^{-1}$) | Density (kg m^{-3}) |
|--------------|--|--|-----------------------------------|
| Brain | 0.55 | 3700 | 1040 |
| Dura-Gel | 0.2 | 840 | 970 |
| Silicon | 148 | 710 | 2330 |
| Sapphire | 40 | 700 | 3980 |
| Glass needle | 1 | 800 | 2500 |

was created to represent the UOA in air and tissue (figure 4(C)). The material property inputs to the model are included in table 1. COMSOL creates a 3D mesh of voxels and solves Fourier's law of heat conduction between mesh elements. The input to the model is the electrical power needed for a desired irradiance at the tip of a needle (taken from the experimental L–I–V curves). We assume 90% of the electrical power goes to heat production and 10% to light generation. μLED drive currents (0.5–100 mA), pulse widths (1–100 ms) and frequencies (1–100 Hz) were modelled, as were multiple (simultaneously illuminated) μLED s. Heat spreads from the μLED source through the device based on the material properties of each component. At the boundary of the modelled region, the temperature was fixed (Dirichlet boundary condition). A brain perfusion rate of $0.51 \text{ kg}^{-1} \text{ min}^{-1}$ was included in the COMSOL model [36]. As light levels tested in this work are low ($<10 \text{ mW mm}^{-2}$), heating due to light absorption is not considered [11]. To allow the accuracy of the model to be further assessed, the temperature at the top of the device encapsulation was monitored throughout the *in vivo* experiments using a FLIR thermal camera.

2.6. *In vivo* testing

The device was tested in the left hemisphere of one sufentanil-anesthetized adult female cynomolgus monkey (*Macaca Fascicularis*). To restrict expression of the excitatory opsin channelrhodopsin-2 (ChR2) and the red reporter protein tdTomato to excitatory neurons, the primary visual cortex (V1) was injected with a mixture of Cre-expressing and Cre-dependent adeno-associated viral vectors carrying the genes for ChR2 and tdTomato (AAV9.CamKII.4.Cre.SV40 and AAV9.CAG.Flex.ChR2.tdTomato, Addgene). Following a post-injection survival period of 9 weeks, to allow for opsin expression, the animal was anaesthetized and prepared for an acute terminal experiment. A full description of the procedure is available elsewhere [37]. The UOA was inserted into the opsin/tdTomato-expressing region of V1 to a depth of approximately 1 mm (the curvature of the visual cortex causes different needle tips to be at different depths) using a high-speed pneumatic electrode inserter system (Blackrock Neurotech). The UOA

used in this study had optrode lengths of 1.5 mm and a 60° tip shape. Electrophysiological recordings were made with a 24-channel linear electrode array (LEA), with an electrode spacing of $100 \mu\text{m}$ and a $300 \mu\text{m}$ distance from the tip to the first electrode (V-Probe, Plexon). The LEA was inserted into the cortex, close to the UOA, in two separate penetrations. The first penetration, P1, was approximately 1 mm from the UOA (nearest μLED —row 8, column 1), inserted to a depth of 2.4 mm. The second penetration, P2, was inserted to a depth of 2.6 mm and angled towards the UOA so that the deeper contacts were approximately $800 \mu\text{m}$ from the UOA (nearest μLED —row 5, column 1), while the more superficial contacts were approximately $900 \mu\text{m}$ from the UOA (nearest μLED - row 6, column 1). A 128-channel recording system (Cerebus, Blackrock Microsystems) was used to record the electrical data. Data were sampled from the 24 channels at 30 kHz. A silicone gel (Dura-Gel, Cambridge NeuroTech) was applied across the exposed cortical surface [38], under-filling the UOA. Finally, GELFOAM (Pfizer) was placed over the implant site to protect the exposed scalp tissue and periodically soaked with saline. Each experiment had the same optical stimulation protocol: Light was pulsed at 5 Hz, with 100 ms pulses for a duration of 1 s, followed by a 1.5–21 s inter-trial interval (longer inter-trial intervals were used at the highest photo-stimulation intensities). For each experiment, approximately 5 min of data was recorded giving 30–45 trials, each with five 100 ms μLED pulses. The μLED drive current, location and number of illuminated μLED s was changed between experiments. Stimulus artefacts often occur when combining optogenetic stimulation and electrical recording. In our case artefacts typically arise from two sources: electrical coupling between the μLED drive lines and recording channels and light induced artefacts due to the Becquerel effect. Since our electrical recording device is not directly integrated with the UOA, electrical cross talk was minimised by the separation between devices ($\sim 800 \mu\text{m}$), good encapsulation and electrical grounding, and ramping the control voltage for the μLED (time constant = $50 \mu\text{s}$). Light induced artefacts are determined by the material properties of the electrode and light intensity [22, 39]. With traditional AC-coupled amplification, they appear within

the first few ms of light switching on and off [39, 40]. As there was a distance of at least 800 μm between our light emitting device and recording electrode, light intensity is greatly attenuated due to scattering and absorption in tissue. No light-induced artifacts were visible in the data presented here (see appendix 3).

On completion of the experiments, the tissue around the device implant site was excised, fixed and underwent histological analysis [37].

All procedures detailed here conformed to the US National Institutes of Health Guide for the Care and Use of Laboratory Animals and were approved by the University of Utah Institutional Animal Care and Use Committee.

2.7. *In vivo* data analysis

Multi-unit activity (MUA) is a high-frequency signal band, often used as a measure of the spiking activity of many neurons in the vicinity of a recording electrode and was observed in response to UOA activation of ChR2-expressing neurons. To assess the level of activation the data was first processed by employing a band stop filter (2nd order Butterworth) to remove 60 Hz interference from mains power. The MUA was quantified by further filtering using a band pass filter from 0.3 kHz to 6 kHz and the absolute value of this signal on each electrode was taken as a function of time. The data from multiple trials was then aligned based on the μLED pulse time and averaged. Low-frequency activity or local field potential (LFP) data can also be extracted using a band pass filter between 1 and 100 Hz. The current source density (CSD) was calculated from the LFP data using a kernel CSD method (kCSD_Matlab [41]). The CSD reveals the location of current sinks (neuron depolarisation) and sources (return currents) throughout the cortical depth. To average the signal from multiple trials, the data was aligned based on the turn-on time of the μLED pulse.

3. Results

3.1. Optical performance

The modelled optical output of the UOA device, with an optical interposer, is shown in figure 2(A). The device has a modelled optical efficiency of 0.4% (the previously reported pinhole device had a modelled efficiency of 0.22% [28]). Due to the silicon optical interposer, the stray light emitted at the base of the needles has also been reduced by a factor of 12 compared to the previous device (figures 2(A) and (B)). Figure 2(C) shows the modelled volume of tissue illuminated with an irradiance of greater than 1 mW mm^{-2} for both the new interposer UOA and the former pinhole device. The interposer device gives an expected volume above a 1 mW mm^{-2} threshold of 2.1 times that of the pinhole device.

The optical models were further used to determine the optimal tip angle for the needle device, with

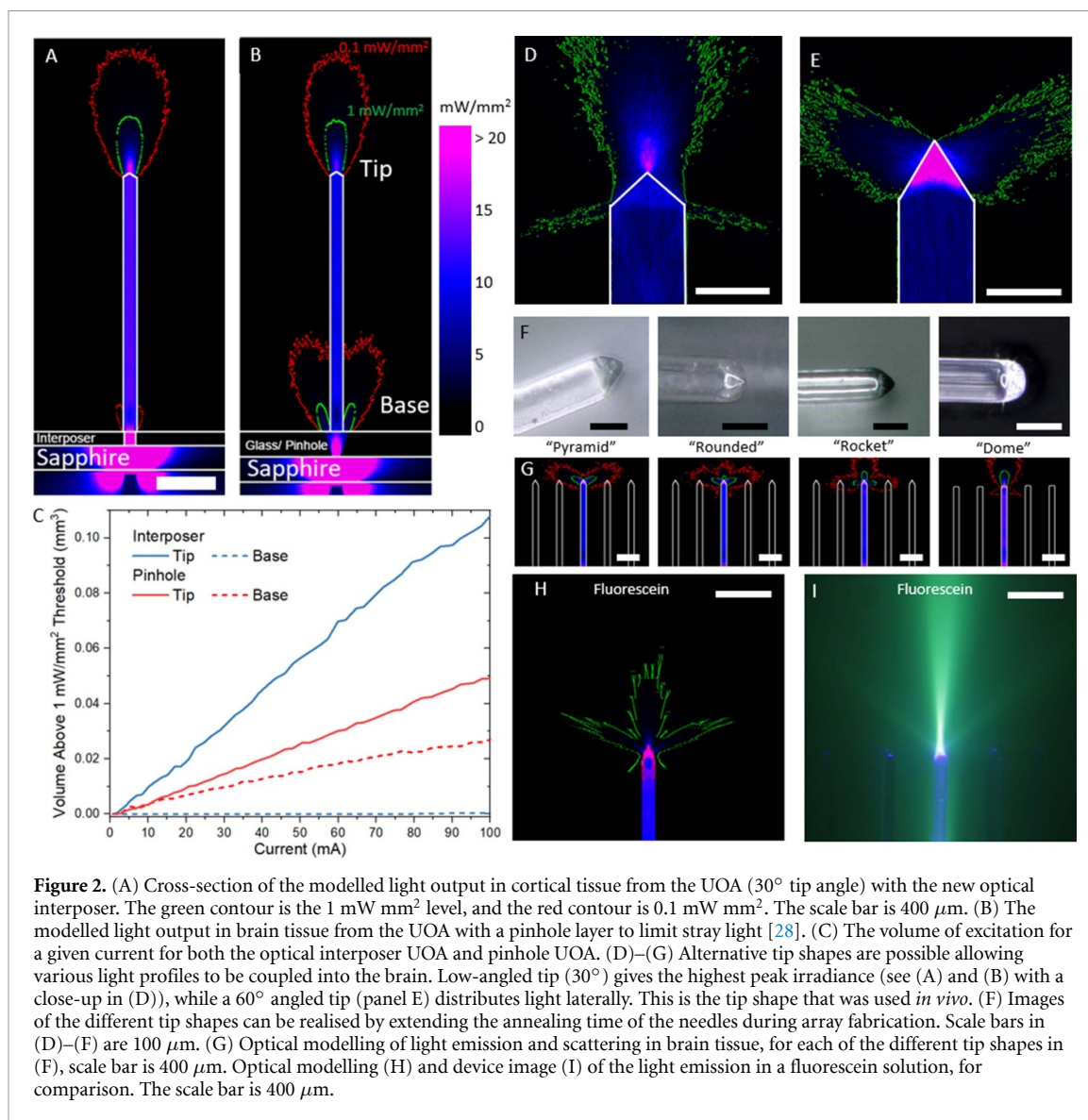
a 30° tip outcoupling most light. However, this is not ideal for device implantation, needles with larger tip angles minimise the insertion force required to penetrate the brain and reduce trauma and vascular damage [42]. Optical modelling indicates that low tip angles (30°) give deep illumination, while large tip angles (>60°) give a lateral profile more suited to laminar optogenetic excitation (figures 2(D) and (E)). Sideways emission is caused by reflected rays, from the glass-brain interface, being out-coupled at the opposite facet. Above a tip angle of 60°, all the light will be directed laterally due to total internal reflection. The device used for the *in vivo* study had a tip angle of 60°.

The tip geometry can be controlled by the bevel angle of the dicing blades, and the heat treatment used to smooth the optrode surface [19]. The annealing step causes a rounding of the corners at the tip of the device. If the annealing time is increased the tip shape becomes more rounded, starting with rounding of the sharp corners of the tips, before transitioning into a rocket tip shape and then into a hemispherical dome shape (figure 2(F)). This had a similar effect to altering the tip angle and can give the device user a pre-determined choice of optical profile depending on the brain region they are targeting (figure 2(G)).

Figures 2(H) and (I) show the modelled and imaged optical output from a test device in a fluorescein solution. This confirms that the optical model captures the light emission profile from the device.

Multiple, simultaneous illumination sites were also modelled (appendix 4), with the magnitude of each μLED output given by measured values for the fabricated device. In this device architecture iteration, the interstitial sites were not coupled to TSVs, as we adopted an iterative approach to device design and had concerns about over-complicating the first fabrication run. These concerns proved unfounded, and we have since made devices with operational interstitial sites (appendix 4), though these have not been tested *in vivo*. Modelling of the interstitial sites indicates that a distance of up to 1 mm, from the surface of the cortex, can be illuminated at an irradiance above 1 mW mm^{-2} .

Figures 3(A) and (B) show the average irradiance output of the device when each μLED is driven at 20 mA after integration with a needle array. The μLED performance before integration is shown in appendix 5. Since a tip angle of 60° was used here, there is a lateral outcoupling of light and no near-field focus (as previously reported [28] and shown in figure 2(D)). For this reason, we do not quote the peak irradiance, but instead give the average irradiance across the emitting area of the tip, as shown in figure 2(E). The non-uniformity in figures 3(A) and (B) in average irradiance is a result of fabrication variances across each μLED . The array uniformity can be

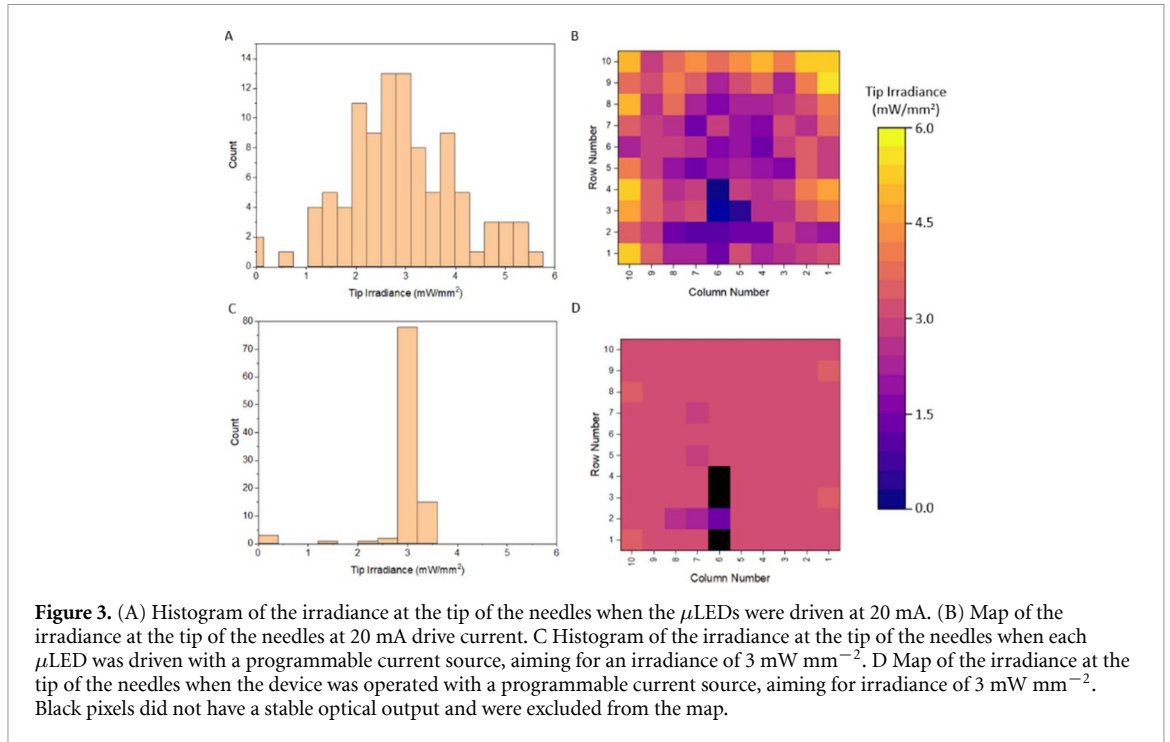


improved by adjusting the current/voltage on a pixel-by-pixel basis. However, the maximum tip irradiance will be set by the least bright μLED included in the adjustment (3 mW mm^{-2} in figures 3(C) and (D)). In this case, 94 out of 100 μLEDs will emit between 3 and 3.4 mW mm^{-2} . This could be improved further by replacing the voltage source used here with a programmable current source with μA steps between current levels. The current and voltage required to achieve uniform illumination are shown in appendix 5.

3.2. Thermal performance

It has been observed that small temperature deviations of $\sim 1^\circ\text{C}$ can change the behaviour of neurons [29]. Temperature changes of this magnitude can also drive changes in behaviour [30]. Previously the thermal constraints when the device was fully inserted were explored and the temperature at the tips of the needles where light is emitted was reported [28].

However, thermal modelling indicates that the temperature at the base of the needles will get significantly warmer and could potentially alter the behaviour of superficial neurons. Here the operating range for the μLEDs is extended by partially inserting the array and underfilling it with a thin layer ($\sim 500 \mu\text{m}$) of silicone (Dura-Gel) between the brain and the device backplane. The primary purpose of this layer is to prevent the surface of the brain from drying out during experiments [38]. Moreover, this thermally insulating layer significantly reduces temperature increases at the cortical surface compared to direct contact between the device and cortical tissue (appendix 6). Figure 4(A) shows the device implanted into the monkey area V1. The Dura-Gel is transparent and not visible in the image. The GELFOAM (labelled) is placed on top of the Dura-Gel and used to prevent the tissue around the scalp from drying out. This is periodically soaked in saline throughout the experiment. Figure 4(B) shows the maximum temperature



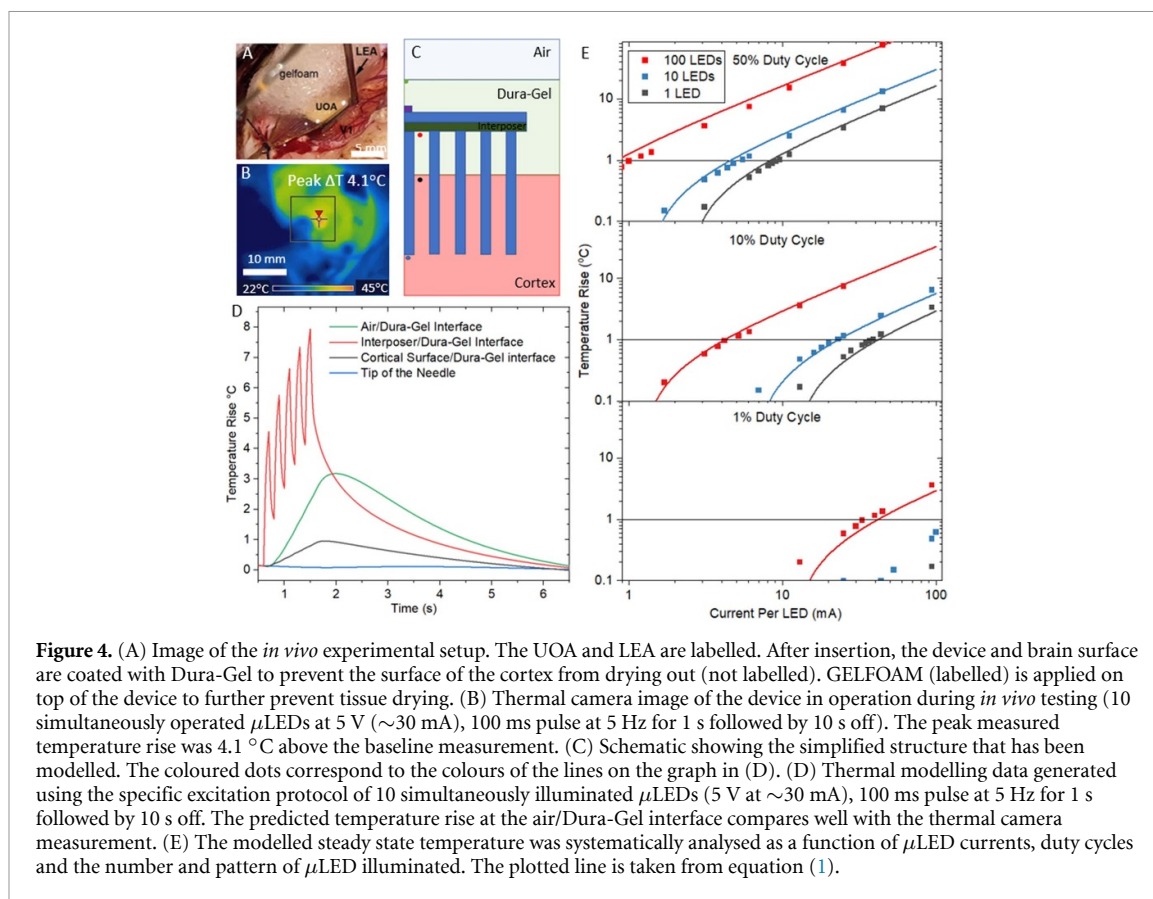
recorded using a thermal camera while the device was operated with 10 simultaneously activated μ LEDs, each operated at 5 V ($\sim 30 \text{ mA}$), 100 ms pulses at 5 Hz for 1 s followed by 10 s off. This measurement gives a $4.1 \text{ }^\circ\text{C}$ temperature rise at the top of the Dura-Gel, which coated the device. From thermal modelling, this surface temperature corresponds to a brain surface temperature increase of $1 \text{ }^\circ\text{C}$. Figure 4(C) shows a schematic of the geometry of the thermal model, the highlighted points are the positions where the modelled temperature is recorded: Green—Air/Dura-Gel boundary; Red—Interposer/Dura-Gel boundary; Black—Cortex/Dura-Gel boundary; Blue—tip of the needle. Though the temperature deviation at the tip is the most obvious location to consider, it is also important to understand the temperature variations at other positions on/near the device in case they too have relevance. Figure- 4(D) shows the temperature of various points on the device for the specific stimulation pattern that was used in the *in vivo* experiments (100 ms pulses at 5 Hz for 1 s followed by 10 s off.). The colours of the lines correspond to the points highlighted in figure 4(C). The green line is at the Dura-Gel/Air boundary and corresponds to the measurement point using the IR camera (figure 4(B)), which reaches a maximum temperature approximately 2 s after the start of the stimulation trial. The difference between these two values (modelled: $3.1 \text{ }^\circ\text{C}$ increase, measured: $4.1 \text{ }^\circ\text{C}$ increase) is likely due to the estimation of the Dura-Gel thickness (taken to be $\sim 300 \text{ }\mu\text{m}$) that lies above the device. Further stimulation protocols are compared in appendix 6, showing good agreement in each case. Although the device itself can increase

in temperature by several degrees during operation, the modelling indicates that the surface of the cortex (black line in figure 4(D)) remains just below $1 \text{ }^\circ\text{C}$ with the tip of the needle (blue line) showing no temperature change for this specific stimulation pattern.

Figure 4(E) shows a more general case of continuously pulsing the μ LEDs at various duty cycles, currents, and number of activated μ LEDs. The quoted temperature here is for the point at which the device reaches a steady-state equilibrium temperature (i.e. where thermal generation by the μ LEDs is balanced by heat dissipation in tissue and through the device). This occurs after approximately 35 s of continuous operation for any given duty cycle. From these results, a linear fit to the data gives a formula which can provide the approximate temperature increase in the brain (ΔT , $^\circ\text{C}$) for a given duty cycle (D), number of μ LEDs (N_{LED}), drive current (I_{LED} , mA) and duration of the pulse train (t , s) (equation (1)).

$$\Delta T \approx \left(\frac{D \cdot I_{\text{LED}}}{3.3} \cdot \left(1 + \frac{N_{\text{LED}}}{10} \right) + \frac{4}{10} \right) H(t) \quad (1)$$

$H(t)$ is a Hill growth function given by $H(t) = t^{1.6}/(6 + t^{1.6})$. For example, setting the maximum temperature rise to $1 \text{ }^\circ\text{C}$ and calculating for 10 μ LEDs, operated at a 10% duty cycle, give a μ LED current limit of 17 mA. This current is sufficient to give an irradiance of 2.5 mW mm^{-2} across the emitting surface of the 60° tipped needle.



3.3. *In vivo* testing

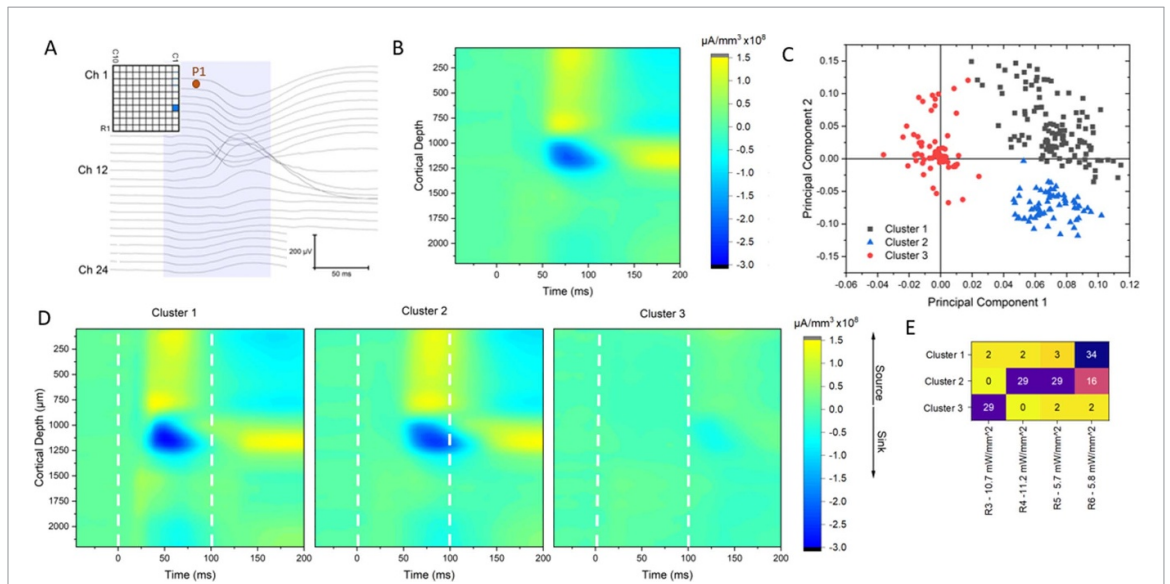
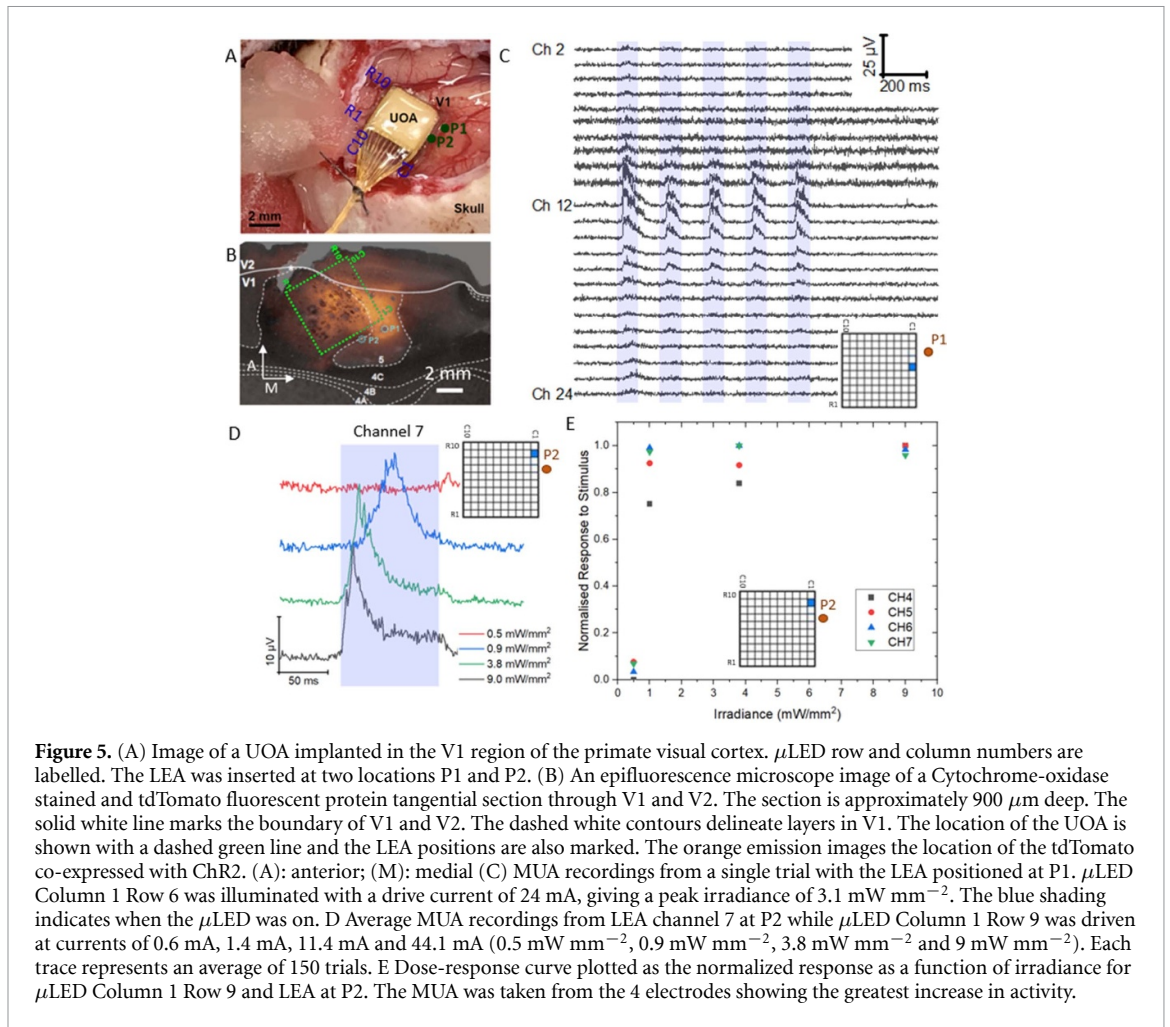
Chr2 and tdTomato were expressed in the macaque visual cortex (V1 and V2) via a mixture of cre-expressing and cre-dependent adeno-associated viral vectors. The UOA was inserted into V1 (figure 5(A)), an area of high expression, that was checked post-experiment through histological imaging of tangential sections (figure 5(B)). After a period of recovery, the LEA was inserted and electrical activity was recorded while the UOA scanned through stimulation protocols.

For each LEA insertion, a strong μ LED dependent increase in MUA could be seen at the approximate location of the tips of the UOA (figure 5(C)), channel 12 in P1 and channel 7 in P2, this corresponds to a cortical depth of 1.1 mm, aligning with layer 4C in the visual cortex. The average response of 150 μ LED pulses on electrode channel 7, while μ LED C1 R9 was illuminated at different irradiances, is shown in figure 5(D). The irradiance is calculated as the average irradiance across the area of the tip where light is emitted. This allows us to create a dose-response curve (figure 5(E)). The onset of optogenetic excitation for this limited experiment was an average tip irradiance of 0.9 mW mm^{-2} .

In figure 6, the LFP and CSD of the optogenetic response (as recorded by the LEA at insertion point P1) are shown and analysed as a function of

which μ LED was activated. The motivation was to assess the distinctiveness of the neural response for different μ LED positions. In figure 6(A) the average LFP response from 31 trials when μ LED C1 R4 was switched on with an average tip irradiance of 11 mW mm^{-2} is shown, this shows a strong positive deflection around channel 12 approximately 50 ms after the onset of the μ LED illumination. In figure 6(B) the CSD calculated from the data in figure 6(A) is shown. This shows a strong current sink in the layer where the tips of the needles were located (point of highest irradiance). The minimum value of the corresponding sink is approximately 75 ms after the onset of the 100 ms duration μ LED illumination.

To demonstrate how different μ LED sites can induce different patterns of LFP response, the individual trials from 4 different μ LEDs were taken (C1-R3, C1-R4, C1-R5 and C1-R6), the CSD for each trial was calculated and a principal component analysis (PCA) was used to determine the statistical variance between the CSD plots, by projecting the data into principal component space. Similar LFP/CSD responses should cluster into distinct regions of the phase space and the correlation of this clustering with μ LED position will give an indication as to the distinctiveness of the induced neural activity. K-means clustering was used on the first 5 principal components to define the clusters (containing $\sim 80\%$ of



the data variability). The data clusters into 3 distinct populations (figure 6(C)), each showing differing neural responses. When plotting the average CSD for each cluster (figure 6(D)): cluster 1, shows the largest response with the shortest latency to the deepest current sink (50 ms); Cluster 2, has a latency that increases to 90 ms and a reduction in the current sink depth; cluster 3 shows a greatly reduced response and an increased latency (125 ms) to the minimum current sink. Which μ LED is responsible for which cluster is examined in the correlogram in figure 6(E). Cluster 1 has 41 entries, 34 of which are from μ LED C1 R6 stimulation (the nearest to the LEA). Cluster 2 has 74 entries, mostly attributed to μ LED C1 R4 and R5 (29 entries each). Cluster 3 has 33 entries, with 29 of them from μ LED C1 R3 (the μ LED furthest from the LEA). This analysis demonstrates that there is a statistically significant difference in the optically induced cortical activity pattern from each μ LED site. As the UOA stimulation sites become more distant, the latency of the current sinks, detected on the LEA, increases. In appendix 7 the statistical difference between each of the clusters that were identified in the PCA analysis is quantified.

4. Discussion

In this work, a glass needle array is integrated with a thin 100 μ m Si interposer, which is directly coupled to a μ LED array, giving a device that is capable of illuminating 181 individually controlled sites across two levels in the cortex. The closer proximity of the μ LED to the glass needle aperture improves the optical efficiency of light delivery to tissue, allowing the device to be operated at significantly lower drive currents, improving the thermal characteristics and light output properties. For example, this approach produces the same optical output power from the needle tips (80 μ W) at half the electrical current of our previous approach (10 mA instead of 20 mA) [28]. This increase in efficiency extends the range over which the device can operate without exceeding thermal limitations. This means an increased irradiance and so an increased volume above a given threshold (e.g. 1 mW mm⁻² for ChR2). It could also mean an increased stimulation duty cycle to better match natural neuronal activity. Implantable μ LED probes can achieve >10% optical efficiency; however, the μ LED source is in contact with delicate and temperature-sensitive neural tissue, meaning that thermal constraints also limit the maximum optical output [13–16]. Further increases in the optical efficiency of the UOA could be achieved by filling the interposer holes with a material that matches the refractive index of the glass needles, further thinning the interposer layer,

designing a top emission μ LED device or integrating micro-lenses to improve optical coupling [41].

The optical interposer also reduced stray light power from the base of the needles for these drive currents (from 85 μ W to 7.2 μ W), allowing single-site activation with reduced cross-talk between epicortical and deep sites. In the previous version of the UOA, a pinhole layer was used to reduce stray light. While this was effective when compared to the case without a pinhole layer, there was still a volume of tissue (\sim 0.007 mm³ when the μ LED is operated at 20 mA) at the surface of the cortex that would be above 1 mW mm⁻² irradiance [28]. This caused some ambiguity about the region where an optogenetic signal was being generated. The UOA with interposer achieves illumination at the tip of the needle with no stray light (above the stimulation threshold) in the superficial layers of the cortex. This new design removes uncertainty in the stimulation region and allows for a greater scope of *in vivo* experiments. Further improvements to remove any residual stray light can also be considered, including coating the base of the needles with an optical absorber.

The output and beam profile from the needle tip can also be modified by changing the bevel angle of the dicing blade or annealing time during the fabrication of the glass needles (figure 2) [24]. If deep illumination is required, a shallow tip angle (\sim 30°) should be used, while if a laminar illumination profile is preferred, a tip angle of \sim 60° is required. It is possible to create Utah slant optrode arrays [43], in which the needle length is ramped across one dimension of the array, where side-emission from a wedged-tip would achieve illumination across multiple depths from a single device.

While fabrication of these devices is technically challenging, they offer some advantages over other multisite, spatially resolved approaches. In primate studies, several different surface illumination strategies are commonly used [19–21]; however, the maximum illumination depth is typically limited to less than 1 mm due to scattering and absorption in brain tissue. Other approaches, include implantation of several optical fibres [27] or the use of a probe with laser-coupled optical waveguides [17, 18, 44], usually require optical alignment of an external source that is challenging to maintain during a behavioural experiment. A further advantage of our approach is that it is electrically addressed, meaning there is a clear pathway to create a wireless, battery-powered device for freely behaving experiments. Implantable probes with μ LEDs directly integrated on the probe [13–16] are also technically challenging to produce but offer the advantage of higher laminar resolution illumination than the device presented here. However, they do not provide light over the broad spatial extent

shown here, which is important for studies in larger mammals [8].

Both the depth and lateral resolution of optogenetic stimulation were investigated as part of the *in vivo* studies. Figures 5(C) and 6(A) both show clearly defined neuronal activity, correlated to the optogenetic stimulation in the location of the UOA needle tips. The depth distribution of evoked activity spans across ~ 6 electrodes, $600\ \mu\text{m}$. No activity (correlated to the optogenetic stimulation) was observed in the most superficial recording sites (less than a depth of $500\ \mu\text{m}$) in either case. The extent of the optogenetically driven activity corresponds well with the optical modelling in figures 2(F) and supplementary figure (A2). Lateral resolution is more difficult to quantify with the current experimental methodology. However, the analysis in figure 6 indicates that each needle site is producing a different pattern of neuronal activity, suggesting that higher-resolution devices may add functionality. Increasing the transverse resolution, by reducing the pitch of the needles, is challenging with the current fabrication approach, particularly since the needle diameter would also likely have to be reduced to minimise brain volume displacement. Thinner needles will reduce optical coupling efficiency and are more likely to break during fabrication, affecting device yield and requiring process optimisation. Alternate methods for producing transparent needle arrays are being investigated including two-photon polymerization [45].

A focus of future research is integrating the light delivery device presented here with recording electrodes. It is possible to pattern the glass optrodes with a conformal coating of metal (similar to [46]) or a transparent conductor (such as indium tin oxide) to form electrical tracks that connect to the base of the needle, where through-silicon-vias route the tracks to the backside of the device for connection to amplification electronics.

Thermal modelling of the device indicates that there is a broad range of drive currents and duty cycles which will not increase the temperature above a $1\ ^\circ\text{C}$ limit. In the previous work [28], the UOA was considered as an isolated device inserted into tissue. In this work, a full system approach is used. A silicone gel (Dura-Gel, Cambridge Neurotech) layer, whose

primary role is to prevent the delicate cortical tissue from drying out [38] is found to also act as a thermal barrier and enhance the operational range of the device. For example, when $10\ \mu\text{LEDs}$ were operated to give an optical output power of $660\ \mu\text{W}$ (sufficient to optogenetically excite neurons expressing ChR2 in a tissue volume of $0.11\ \text{mm}^3$) the previous approach had a thermally imposed duty cycle limit of 7%, which is extended to 25% with this new generation device. These increases in the duty cycle and device performance greatly expand the scope of *in vivo* studies that can be pursued [37]. The bond wires used to drive the μLEDs were found to act as a route for heat conduction away from the device, thereby reducing the thermal energy reaching the cortical surface. This points to further improvements that could be made to the device, including an improved thermal barrier between the device and the cortical surface, and intentionally using integrated approaches, that optimize thermal conduction away from the device.

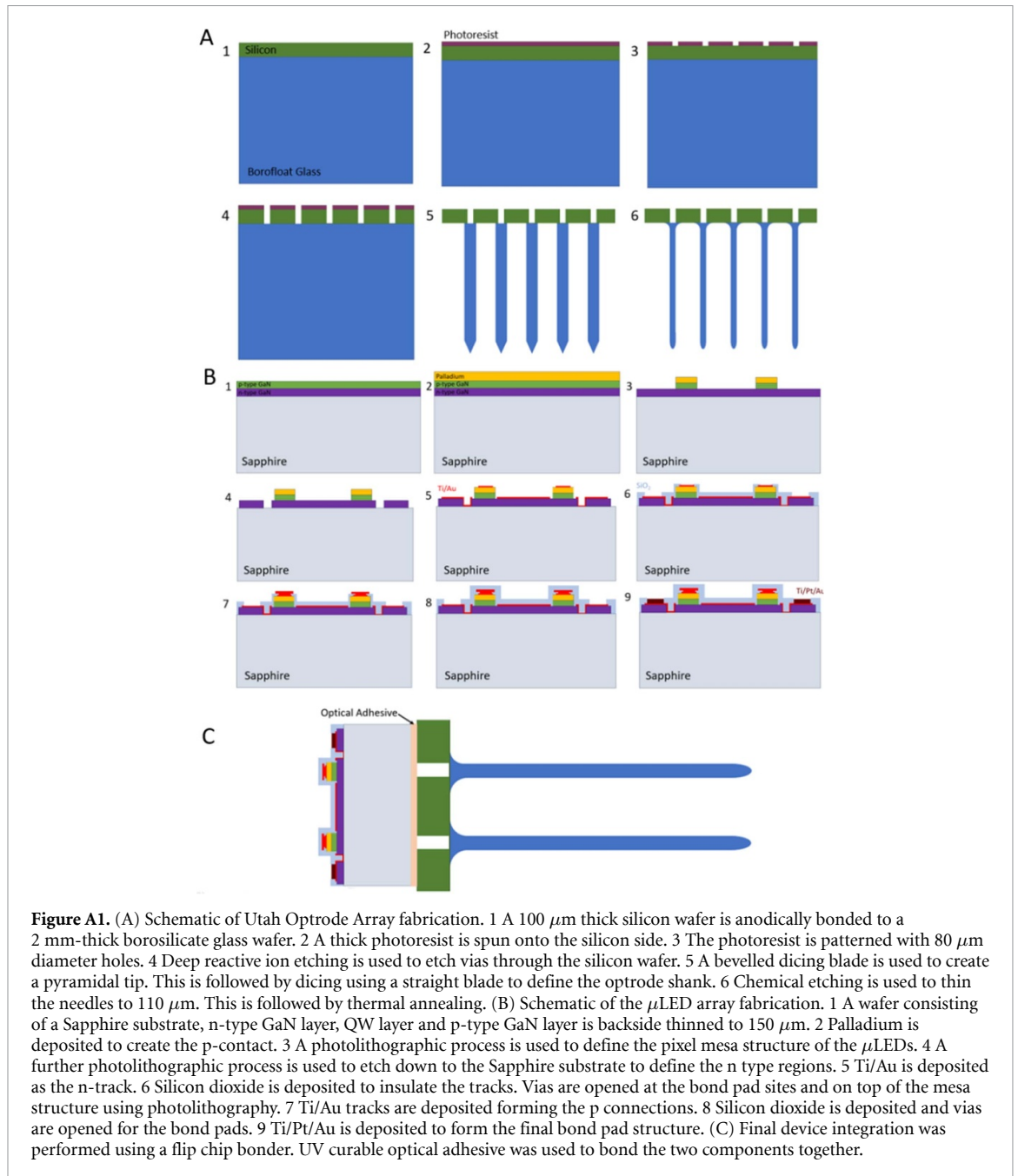
Data availability statement

All data that support the findings of this study are included within the article (and any supplementary files).

Acknowledgments

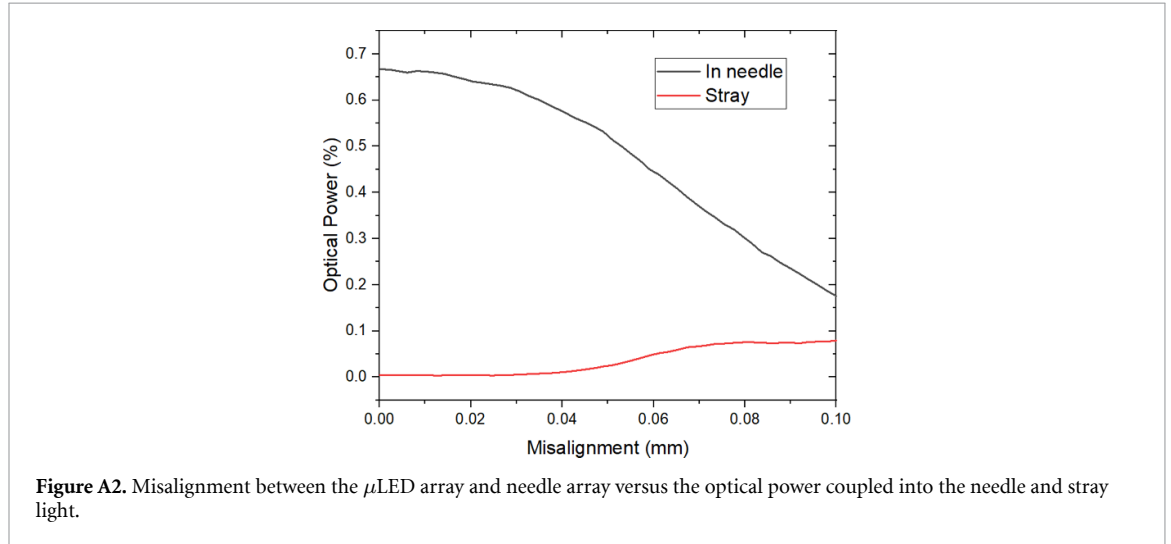
We thank Julian Haberland and Christine Kallmayer at the Fraunhofer-Institut für Zuverlässigkeit und Mikrointegration for μLED -to-interposer bonding. The fabrication of the interposer array was performed at the Utah Nanofab facility. The authors appreciate the support of the Utah Nanofab staff. This work was supported by the NIH BRAIN Initiative through Grant No. U01 NS099702. AA was further supported by the NIH (R01 EY026812; R01 EY031959), the National Science Foundation (IOS 1755431) and the Mary Boesche endowed Professorship; an unrestricted grant from Research to Prevent Blindness, Inc. and a core grant from the NIH (P30 EY014800) to the Department of Ophthalmology, University of Utah. KM was also supported by the Royal Academy of Engineering under the Chair in Emerging Technologies scheme.

Appendix 1



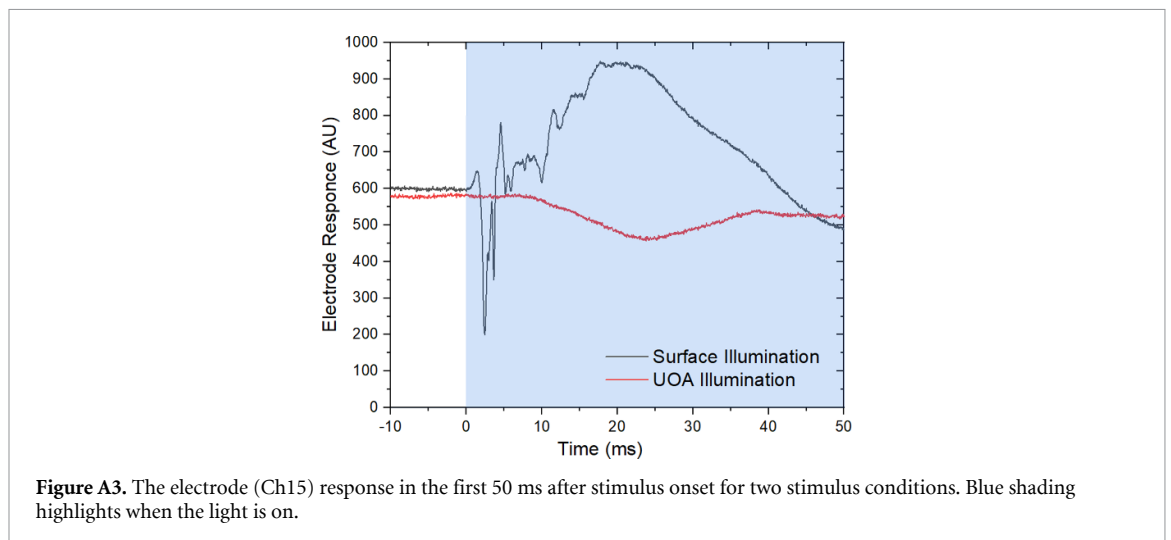
Appendix 2

Misalignment between the μ LED array and UOA can be optically modelled to determine its effect on light coupled into the needle and stray light (figure A2). From this analysis, the misalignment tolerance between the μ LED array and interposer needle array is approximately 20 μ m.



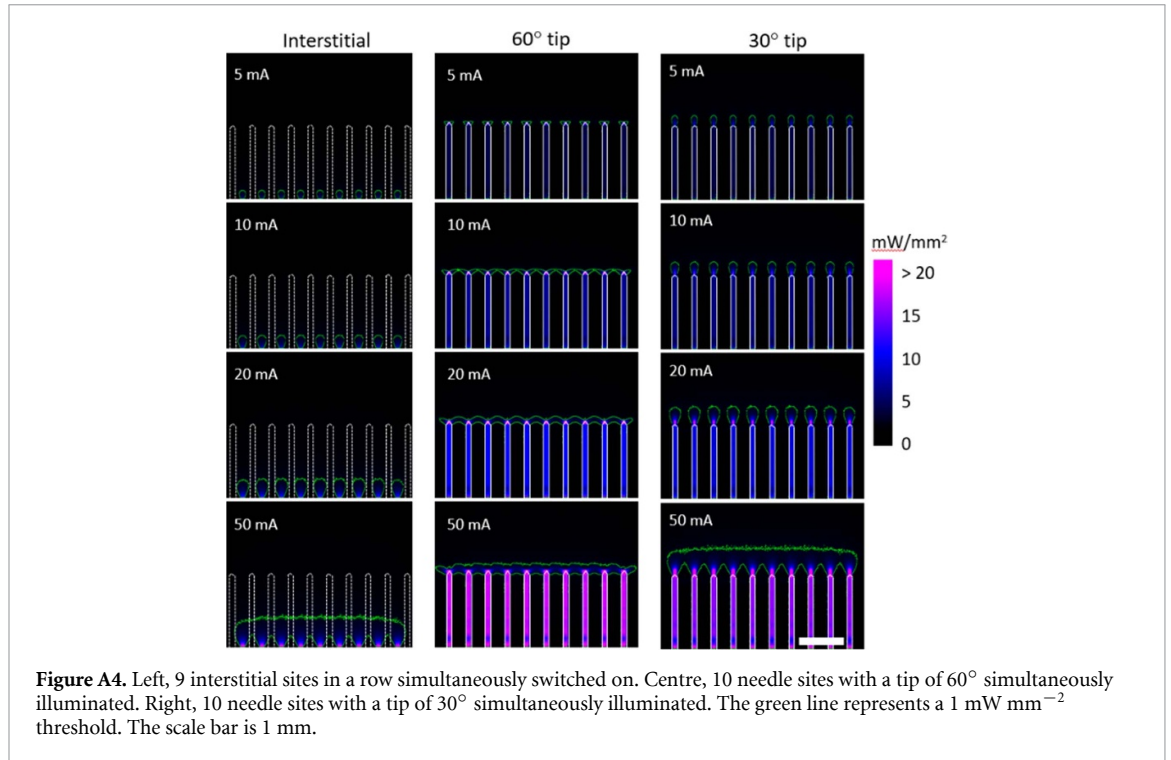
Appendix 3

Figure A3 shows the average electrode response from channel 15 in the first 50 ms after stimulus onset (average of 300 stimulation pulses). In this case, the electrode response is the raw electrode trace, which has been notch-filtered to remove 60 Hz interference from mains power. A further band pass filter (3 Hz–7.5 kHz) is used to remove low-frequency oscillations. The electrode is illuminated in two conditions. A 400 μ m diameter 0.15 NA fibre optic is placed near the surface of the brain illuminating the tissue adjacent to the recording electrode probe and with an irradiance of approximately 20 mW mm^2 . A clear optically induced artefact is visible, reaching a maximum amplitude 3 ms after light onset, indicating that optically-induced voltage deflections occur if the irradiance levels are high. In the second condition, μ LED R9C1 is illuminated at 30 mA (5 V), giving an irradiance at the tip of the optrode of 10 mW mm^2 , which falls to approximately 0.02 mW mm^2 at the electrode site (obtained from optical model). The low irradiance levels at the electrode surface mean that no stimulus artefacts are visible.



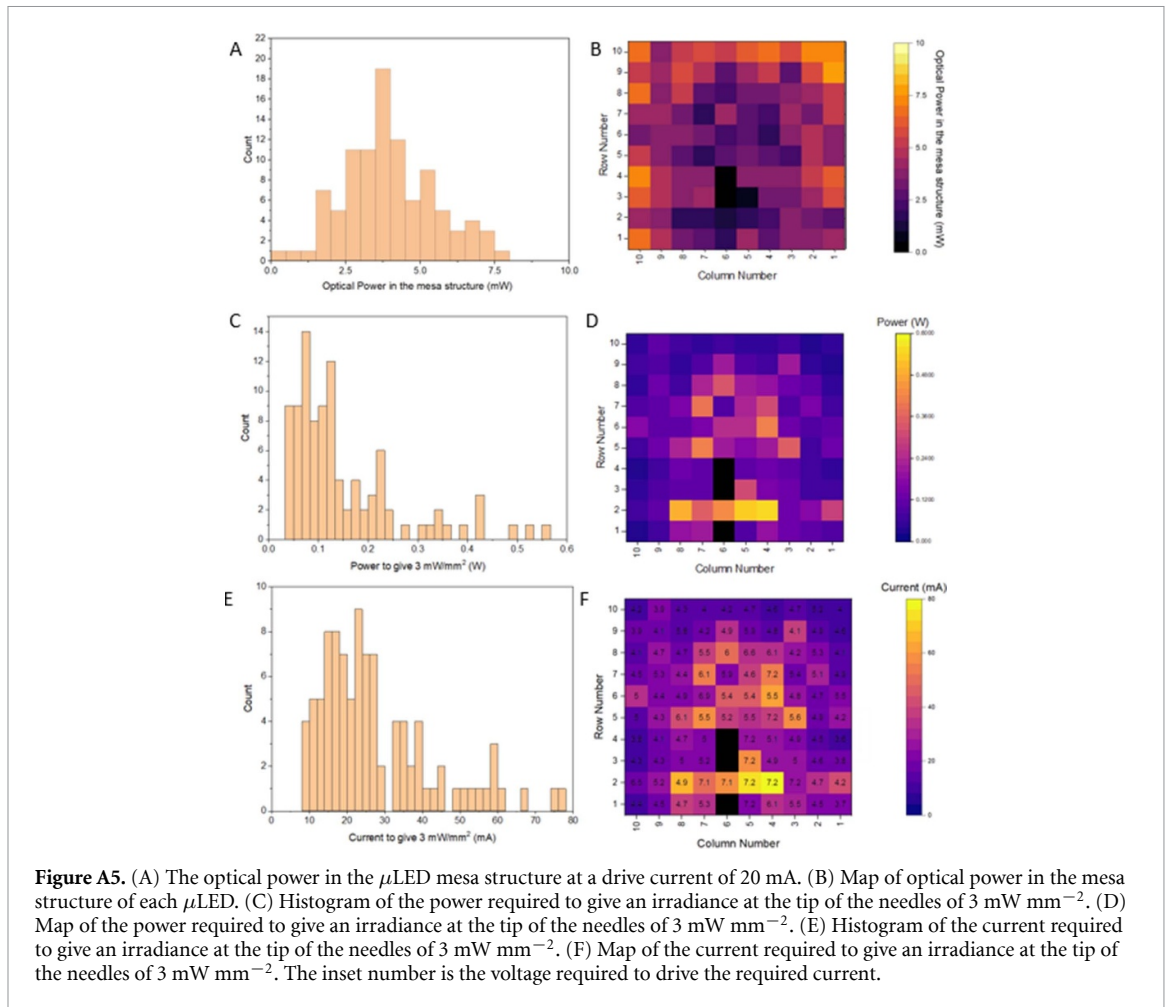
Appendix 4

The emission from multiple simultaneously illuminated sites can be modelled by taking the emission from a single site, duplicating it, shifting it in x or y and summing it with the original model of a single emission site. Figure A4 shows the emission from several sites illuminated simultaneously.



Appendix 5

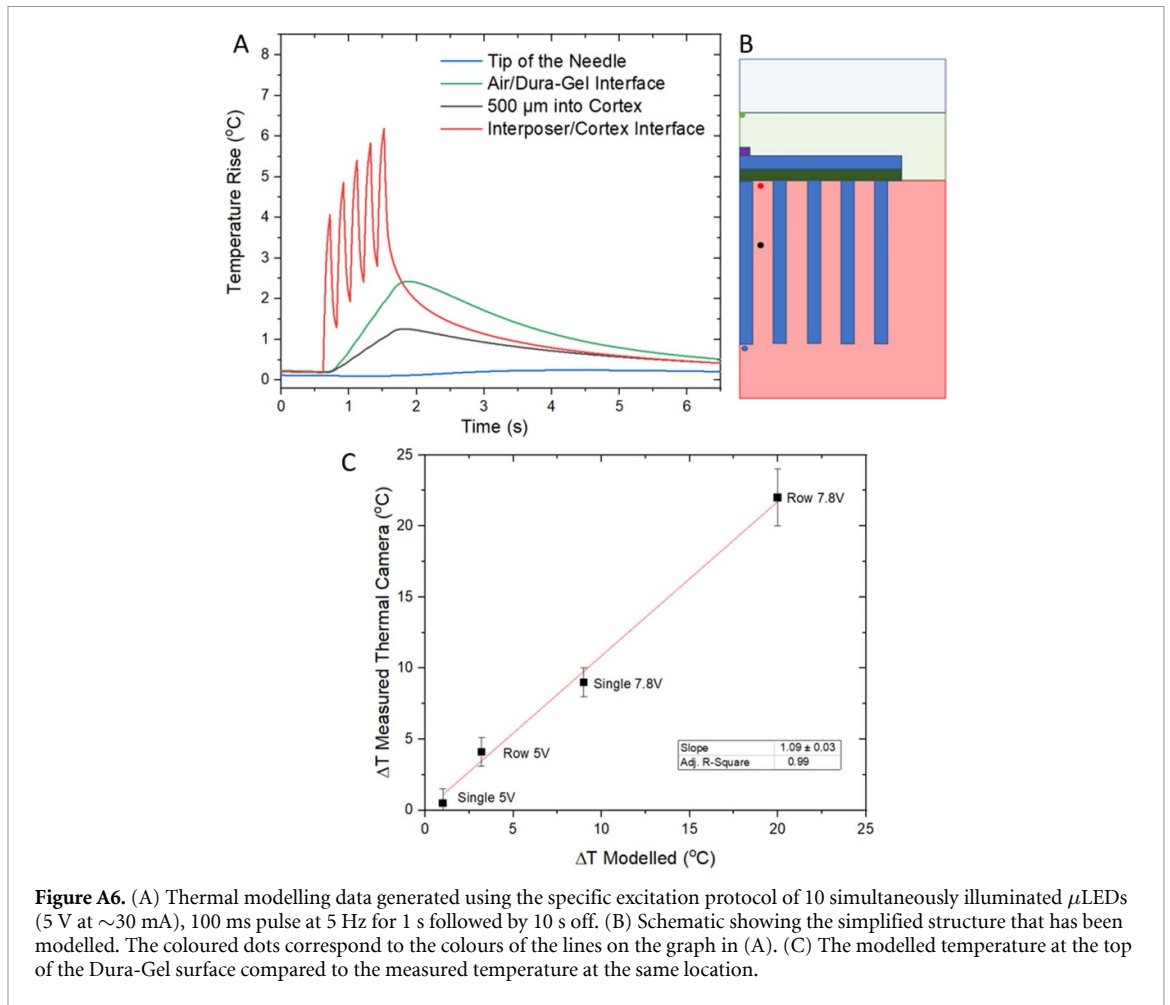
The device was tested before and after integration. Before integration, a geometrical correction factor was used to convert the power measured on an optical power meter to the optical power generated in the mesa structure of the μLED . The optical power in the mesa structure at 20 mA drive current is shown in Figures A4(A) and (B). If equal irradiance is required from each needle tip the power that each μLED is driven at will differ. Figures A5(C)–(F) show the power, current and voltage required for each individual μLED to output 3 mW mm^{-2} .



Appendix 6

Figure A6 A highlights that without the $500 \mu\text{m}$ of Dura-Gel under the device the cortical surface will rise by up to 6 degrees when the device is operated with the same protocol as figure 4(D) (10 simultaneously illuminated μ LEDs (5 V at $\sim 30 \text{ mA}$), 100 ms pulse at 5 Hz for 1 s followed by 10 s off). By $500 \mu\text{m}$ into the cortex, the temperature of brain tissue will not rise by more than 1°C .

The thermal model was verified by comparing the measured temperature of the surface of the Dura-Gel coating directly above the μ LED with the modelled temperature at the same location. The two temperature increases show good agreement for the four cases that were compared (figures A6(C)). Note that this is not the temperature rise in the brain, which is much smaller and quantified in figure 4. The modelled Dura-Gel thickness can have a significant effect on the temperature at the surface of the device (the point where the thermal camera measures). In the models presented here, the total Dura-Gel thickness was taken as 1g mm ($500 \mu\text{m}$ under the device, $230 \mu\text{m}$ device thickness and $270 \mu\text{m}$ on top of the device). This value was not accurately measured but estimated by analysing images after the *in vivo* study was completed.



Appendix 7

A statistical analysis of the difference between the 3 different clusters identified in the PCA is shown in figure A7 and tables A1 and A2.

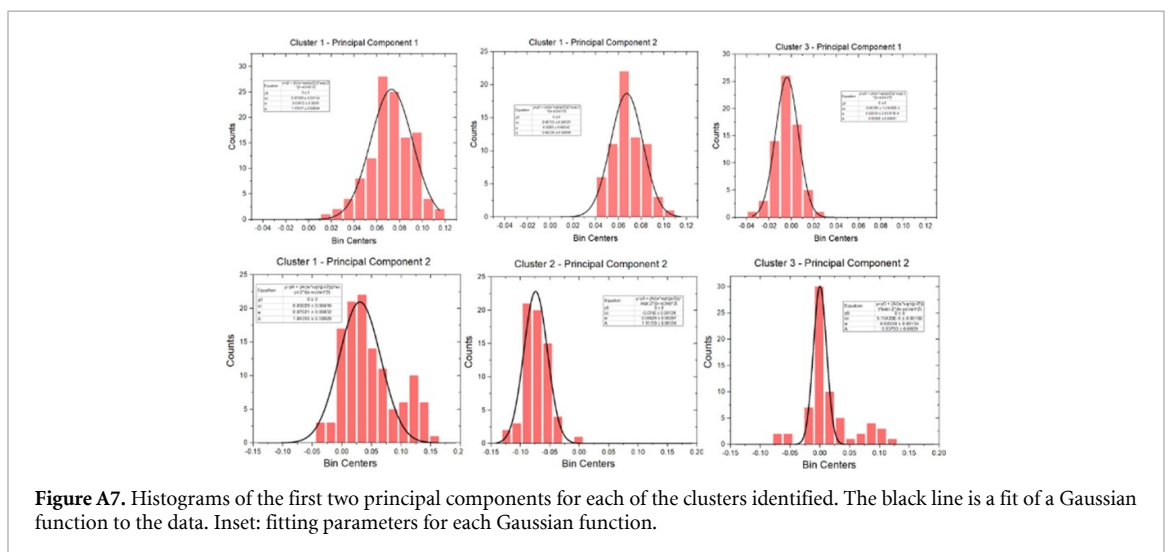


Table A1. Peak position and FWHM for each of the Gaussian fits.

| Principal component 1 | | |
|-----------------------|----------------|----------------|
| | Peak position | FWHM |
| Cluster 1 | 0.073 ± 0.001 | 0.037 ± 0.003 |
| Cluster 2 | 0.067 ± 0.001 | 0.028 ± 0.002 |
| Cluster 3 | 0.004 ± 0.0001 | 0.02 ± 0.0003 |
| Principal component 2 | | |
| Cluster 1 | 0.03 ± 0.004 | 0.07 ± 0.006 |
| Cluster 2 | -0.074 ± 0.001 | 0.04 ± 0.002 |
| Cluster 3 | 0.000 ± 0.001 | 0.022 ± 0.0002 |

Table A2. Number of sigmas between each peak in the Gaussian fit. In this case, the sigma value was taken as the average of the sigma from each of the two Gaussian fits. This highlights that there is a large statistical difference between each of the 3 clusters identified.

| Principal Component 1—Sigma | | | |
|-----------------------------|-----------|-----------|-----------|
| | Cluster 1 | Cluster 2 | Cluster 3 |
| Cluster 1 | | 0.5 | 5.9 |
| Cluster 2 | | | 6.1 |
| Cluster 3 | | | |
| Principal component 2—Sigma | | | |
| | Cluster 1 | Cluster 2 | Cluster 3 |
| Cluster 1 | | 4.2 | 1.4 |
| Cluster 2 | | | 5.7 |
| Cluster 3 | | | |

ORCID iDs

Niall McAlinden  <https://orcid.org/0000-0002-0369-8788>

Christopher F Reiche  <https://orcid.org/0000-0001-6216-5888>

Martin D Dawson  <https://orcid.org/0000-0002-6639-2989>

Keith Mathieson  <https://orcid.org/0000-0002-9517-8076>

References

- [1] Ryan T J, Roy D S, Pignatelli M, Arons A and Tonegawa S 2015 Memory. Engram cells retain memory under retrograde amnesia *Science* **348** 1007–13
- [2] Sahel J-A *et al* 2021 Partial recovery of visual function in a blind patient after optogenetic therapy *Nat. med.* **27** 1223–9
- [3] Emiliani V *et al* 2022 Optogenetics for light control of biological systems *Nat. Rev. Methods Primers* **2** 55
- [4] Jiang S, Wu X, Rommelfanger N J, Ou Z and Hong G 2022 Shedding light on neurons: optical approaches for neuromodulation *Natl Sci. Rev.* **9** nwac007
- [5] El-Shamayleh Y and Horwitz G D 2019 Primate optogenetics: progress and prognosis *Proc. Natl Acad. Sci.* **116** 26195–203
- [6] Tremblay S *et al* 2020 An open resource for non-human primate optogenetics *Neuron* **108** 1075–90.e6
- [7] Diester I, Kaufman M T, Mogri M, Pashaie R, Goo W, Yizhar O, Ramakrishnan C, Deisseroth K and Shenoy K V 2011 An optogenetic toolbox designed for primates *Nat. Neurosci.* **14** 387–97
- [8] Merlin S and Vidyasagar T 2023 Optogenetics in primate cortical networks *Front. Neuroanat.* **17** 1193949
- [9] Galvan A, Stauffer W R, Acker L, El-Shamayleh Y, Inoue K-I, Ohayon S and Schmid M C 2017 Nonhuman primate optogenetics: recent advances and future directions *J. Neurosci.* **37** 10894–903
- [10] Acker L C, Pino E N, Boyden E S and Desimone R 2017 Large volume, behaviorally-relevant illumination for optogenetics in non-human primates *J. Vis. Exp.* **128** e56330
- [11] Senova S, Scisniak I, Chiang C-C, Doignon I, Palfi S, Chaillet A, Martin C and Pain F 2017 Experimental assessment of the safety and potential efficacy of high irradiance photostimulation of brain tissues *Sci. Rep.* **7** 43997
- [12] Kim T I *et al* 2013 Injectable, cellular-scale optoelectronics with applications for wireless optogenetics *Science* **340** 211–6
- [13] Klein E, Gossler C, Paul O and Ruther P 2018 High-density μ LED-based optical cochlear implant with improved thermomechanical behavior *Front. Neurosci.* **12** 659
- [14] Scharf R, Tsunematsu T, McAlinden N, Dawson M D, Sakata S and Mathieson K 2016 Depth-specific optogenetic control in vivo with a scalable, high-density μ LED neural probe *Sci. Rep.* **6** 28381
- [15] Wu F, Stark E, Ku P-C, Wise K, Buzsáki G and Yoon E 2015 Monolithically integrated μ LEDs on silicon neural probes for high-resolution optogenetic studies in behaving animals *Neuron* **88** 1136–48
- [16] Vöröslakos M *et al* 2022 HectoSTAR μ LED optoelectrodes for large-scale, high-precision in vivo opto-electrophysiology *Adv. Sci.* **9** 2105414
- [17] Hoffman L *et al* 2015 High-density optrode-electrode neural probe using SixNy photonics for in vivo optogenetics 2015 *IEEE Int. Electron Devices Meeting (IEDM)* pp 29.5.1–4
- [18] Sacher W D *et al* 2019 Visible-light silicon nitride waveguide devices and implantable neurophotonic probes on thinned 200 mm silicon wafers *Opt. Express* **27** 37400–18
- [19] Zaraza D, Chernov M M, Yang Y, Rogers J A, Roe A W and Friedman R M 2022 Head-mounted optical imaging and

- optogenetic stimulation system for use in behaving primates *Cell Rep. Methods* **2** 100351
- [20] Ruiz O, Lustig B R, Nassi J J, Cetin A, Reynolds J H, Albright T D, Callaway E M, Stoner G R and Roe A W 2013 Optogenetics through windows on the brain in the nonhuman primate *J. Neurophysiol.* **110** 1455–67
- [21] Yazdan-Shahmorad A, Diaz-Botia C, Hanson T, Kharazia V, Ledochowitsch P, Maharbiz M and Sabes P 2016 A large-scale interface for optogenetic stimulation and recording in nonhuman primates *Neuron* **89** 927–39
- [22] Nurminen L, Merlin S, Bijanzadeh M, Federer F and Angelucci A 2018 Top-down feedback controls spatial summation and response amplitude in primate visual cortex *Nat. Commun.* **9** 2281
- [23] Rajalingham R, Sorenson M, Azadi R, Bohn S, DiCarlo J J and Afraz A 2021 Chronically implantable LED arrays for behavioral optogenetics in primates *Nat. Methods* **18** 1112–6
- [24] Abaya T V F, Blair S, Tathireddy P, Rieth L and Solzbacher F 2012 A 3D glass optrode array for optical neural stimulation *Biomed. Opt. Express* **3** 3087–104
- [25] Lee J, Ozden I, Song Y-K and Nurmikko A V 2015 Transparent intracortical microprobe array for simultaneous spatiotemporal optical stimulation and multichannel electrical recording *Nat. Methods* **12** 1157–62
- [26] Afraz A 2023 Behavioral optogenetics in nonhuman primates; a psychological perspective *Curr. Res. Neurobiol.* **5** 100101
- [27] Eriksson D, Schneider A, Thirumalai A, Alyahyay M, de la Crompe B, Sharma K, Ruther P and Diester I 2022 Multichannel optogenetics combined with laminar recordings for ultra-controlled neuronal interrogation *Nat. Commun.* **13** 985
- [28] McAlinden N *et al* 2019 Multisite microLED optrode array for neural interfacing *Neurophotonics* **6** 035010
- [29] Acharya A R *et al* 2021 In vivo blue light illumination for optogenetic inhibition: effect on local temperature and excitability of the rat hippocampus *J. Neural Eng.* **18** 066038
- [30] Owen S F, Liu M H and Kreitzer A C 2019 Thermal constraints on in vivo optogenetic manipulations *Nat. Neurosci.* **22** 1061–5
- [31] Yaroslavsky A N, Schulze P C, Yaroslavsky I V, Schober R, Ulrich F and Schwarzaier H-J 2002 Optical properties of selected native and coagulated human brain tissues in vitro in the visible and near infrared spectral range *Phys. Med. Biol.* **47** 2059
- [32] Binzoni T, Leung T S, Gandjbakhche A H, Rüfenacht D and Delpy D T 2006 The use of the Henyey–Greenstein phase function in Monte Carlo simulations in biomedical optics *Phys. Med. Biol.* **51** N313
- [33] Boutte R W and Blair S 2016 Maskless wafer-level microfabrication of optical penetrating neural arrays out of soda-lime glass: utah Optrode Array *Biomed. Microdevices* **18** 115
- [34] Scharf R *et al* 2018 A compact integrated device for spatially selective optogenetic neural stimulation based on the Utah Optrode Array *Proc. SPIE* **10482** 104820M
- [35] Lee Y-C, Ni C-H and Chen C-Y 2010 Enhancing light extraction mechanisms of GaN-based light-emitting diodes through the integration of imprinting microstructures, patterned sapphire substrates, and surface roughness *Opt. Express* **18** A489–98
- [36] Lassen N A 1985 Normal average value of cerebral blood flow in younger adults is 50 ml/100 g/min *J. Cereb. Blood Flow Metab.* **5** 347–9
- [37] Clark A M *et al* 2024 An optrode array for spatiotemporally precise large-scale optogenetic stimulation of deep cortical layers in non-human primates *Commun. Biol.* **7** 329
- [38] Jackson N and Muthuswamy J 2008 Artificial dural sealant that allows multiple penetrations of implantable brain probes *J. Neurosci. Methods* **171** 147–52
- [39] Kozai T D Y and Vazquez A L 2015 Photoelectric artefact from optogenetics and imaging on microelectrodes and bioelectronics: new challenges and opportunities *J. Mater. Chem. B* **3** 4965–78
- [40] Kim K, Vöröslakos M, Seymour J P, Wise K D, Buzsáki G and Yoon E 2020 Artifact-free and high-temporal-resolution in vivo opto-electrophysiology with microLED optoelectrodes *Nat. Commun.* **11** 2063
- [41] Potworowski J, Jakuczun W, Łęski S and Wójcik D 2012 Kernel current source density method *Neural Comput.* **24** 541–75
- [42] Obaid A *et al* 2020 Ultra-sensitive measurement of brain penetration mechanics and blood vessel rupture with microscale probes *bioRxiv Preprint* (<https://doi.org/10.1101/2020.09.21.306498>)
- [43] Abaya T V F, Diwekar M, Blair S, Tathireddy P, Rieth L, Clark G A and Solzbacher F 2012 Characterization of a 3D optrode array for infrared neural stimulation *Biomed. Opt. Express* **3** 2200–19
- [44] Neutens P *et al* 2023 Dual-wavelength neural probe for simultaneous opto-stimulation and recording fabricated in a monolithically integrated CMOS/photonics technology platform 2023 *Int. Electron Devices Meeting (IEDM)* (<https://doi.org/10.1109/IEDM45741.2023.10413839>)
- [45] Gittard S D, Ovsianikov A, Chichkov B N, Doraiswamy A and Narayan R J 2010 Two-photon polymerization of microneedles for transdermal drug delivery *Expert Opin. Drug Deliv.* **7** 513–33
- [46] Campbell P K, Jones K E, Huber R J, Horch K W and Normann R A 1991 A silicon-based, three-dimensional neural interface: manufacturing processes for an intracortical electrode array *IEEE Trans. Biomed. Eng.* **38** 758–68